Journal of Power Sources 658 (2025) 238225

Contents lists available at ScienceDirect

Journal of Power Sources

journal homepage: www.elsevier.com/locate/jpowsour

Conjugated anthraquinone-linked microporous polymers with enhanced energy storage performance

Shimaa Abdelnaser [a,b], Shiao-Wei Kuo [a], Ahmed F.M. EL-Mahdy [a,b,*]

[a] Department of Materials and Optoelectronic Science, National Sun Yat-Sen University, Kaohsiung, 80424, Taiwan
[b] Chemistry Department, Faculty of Science, Assiut University, Assiut, 71516, Egypt

HIGHLIGHTS

- Pyridine- and anthraquinone-based CMPs developed for supercapacitors.
- CMPs achieved a high conductivity of 4.26 S/cm and a capacitance of 632.8 F g^{-1}.
- Symmetric device showed capacitance of 119.6 F g^{-1} and energy density of 23.9 Wh/kg.
- Excellent cycling stability with 84.3 % retention over 10,000 cycles.
- CMPs exhibit promising potential for high-performance energy storage.

GRAPHICAL ABSTRACT

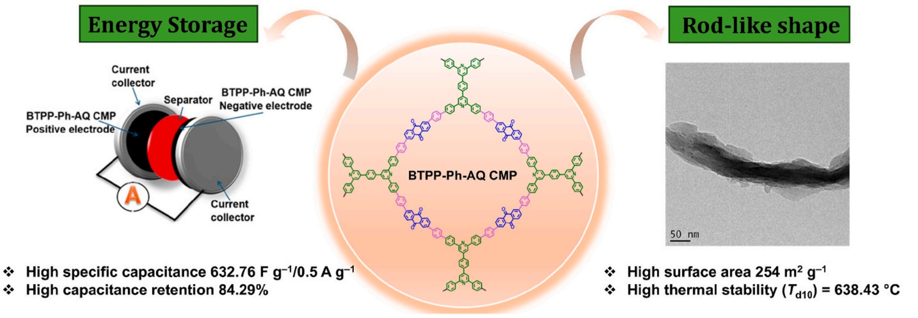

ARTICLE INFO

Keywords:
Anthraquinone
Conjugated microporous polymers
Redox-active materials
Heteroatom-rich
Supercapacitors

ABSTRACT

Conjugated microporous polymers (CMPs) boast high surface area, adjustable properties, and resilience, making them ideal for energy storage. In this work, we succeeded in creating a pair of CMPs with 1,4-bis(2,6-diphenylpyridin-4-yl)benzene (BTPP) and anthracene-9,10-dione (AQ) moieties, namely BTPP-Ph-AQ and BTPP-BPh-AQ CMPs, through one-pot Suzuki coupling polymerization. BTPP-Ph-AQ CMP was synthesized through the combination of 1,4-bis(2,6-bis(4-bromophenyl)pyridin-4-yl)benzene (BTPP-4Br), 1,4-phenylenediboronic acid (Ph-2BO), and redox-active 2,6-dibromoanthracene-9,10-dione (AQ-2Br), while BTPP-BPh-AQ CMP was synthesized by combining (BTPP-4Br), 1,1′-biphenyl-4,4′-boronic acid (BPh-2BO), and (AQ-2Br). Our synthesized CMPs demonstrated elevated surface area (up to about 254 $m^2\ g^{-1}$) and significant thermal stability. High surface area, planarity, and heteroatoms (i.e. active sites) allowed efficient energy storage. The BTPP-Ph-AQ CMP achieved the maximum specific capacity for CMP with a three-electrode capacitance of 632.76 F g^{-1} at 0.5 A g^{-1} and 84.29 % stability over 10,000 cycles. Using BTPP-Ph-AQ CMP, the two-electrode symmetric supercapacitor equipment achieved 119.61 F g^{-1} specific capacitance and 23.92 Wh kg^{-1} maximum energy density. These findings demonstrate an effective method for producing economical heteroatom-enriched conjugated microporous polymers with hierarchical porosity for energy storage purposes.

---

* Corresponding author. Department of Materials and Optoelectronic Science, National Sun Yat-Sen University, Kaohsiung, 80424, Taiwan.
E-mail address: ahmedelmahdy@mail.nsysu.edu.tw (A.F.M. EL-Mahdy).

https://doi.org/10.1016/j.jpowsour.2025.238225
Received 3 February 2025; Received in revised form 8 July 2025; Accepted 22 August 2025
Available online 6 September 2025
0378-7753/© 2025 Elsevier B.V. All rights reserved, including those for text and data mining, AI training, and similar technologies.

1. Introduction

Energy demand and supply are unevenly distributed globally, leading to a significant global challenge [1]. The combustion of fossil fuels in the presence of oxygen releases greenhouse gases, contributing to environmental pollution, accelerating global warming, and harming ecosystems [2]. In response to these challenges, many countries have actively supported and invested in developing renewable and clean energy technologies [3–5]. Examples include solar, nuclear, and wind energy, as well as energy storage systems like supercapacitors (SCs) [6]. Supercapacitors (SCs), also known as ultracapacitors or electrochemical capacitors, offer high power density, greater energy density than conventional capacitors, and rapid charge/discharge capabilities. They operate through reversible electrochemical processes at the electrode-electrolyte interface, enabling swift energy delivery during power fluctuations or outages [7]. There are two primary mechanisms for energy storage in supercapacitors (SCs). The first is electric double-layer capacitance (EDLC), which stores energy through electrostatic charge separation at the electrode-electrolyte interface. The second is pseudocapacitance, which involves fast and reversible faradaic (redox) reactions that contribute additional energy storage. Together, these mechanisms enhance the overall capacitance and performance of SCs [8,9]. Thus, the choice of electrode materials is crucial for enhancing the performance of supercapacitors [10–12]. Despite limited electroactive sites, carbon-based materials are preferred for EDLC electrodes due to their high surface area, good conductivity, and chemical stability. However, they suffer from low energy density and limited conductivity [13,14]. Pseudocapacitive materials—such as conductive polymers, metal sulfides, and transition-metal oxides—store charge via reversible faradaic redox reactions, enhancing supercapacitor energy density [15,16]. However, repeated ion intercalation and deintercalation can cause mechanical instability, limiting electrolyte access to active sites and reducing capacitance and efficiency [17]. The capacity, cyclic stability, and ion/electron transport in metal sulfides and transition-metal oxides have been enhanced by reducing particle size to the nanoscale for increased surface area, doping or adding elements to modify electronic properties and boost conductivity and stability, and integrating them with conductive matrices like carbon materials [16,18–20]. The coupling of carbon-based materials with pseudocapacitive elements signifies substantial progress in creating high-performance energy storage systems [11,21,22]. These options enhance energy density despite affecting rate capability, power density, and cycling durability [23]. To optimize these properties and achieve efficient SCs, electrode materials must have high conductivity, controlled porosity designs, stable topologies, and redox-active moieties.

Conjugated microporous polymers (CMPs) are a unique class of porous organic polymers (POPs) with pore diameters extending from the microporous to the mesoporous range, extensively conjugated π-systems, high surface area, and adjustable structure and functionality [24,25]. Their inherent conductivity and thermal and chemical stability make them ideal for a wide range of applications, including gas storage, separation, catalysis, and energy storage [26]. The synthesis of CMPs using C–N and C–C coupling processes includes numerous essential approaches that enable the development of porous and conjugated topologies [27–29]. These reactions include Suzuki, Sonogashira, Yamamoto, oxidative polymerization, cyclotrimerization, phenazine ring fusion, Buchwald amination, and Schiff base reactions [30–32]. While CMPs offer many advantageous features, they face several challenges that could limit their practical applications, including low cycling durability, poor electronic conductivity, capacity limitations, and restrictions on practical use [33,34]. Many solutions are being investigated to tackle these difficulties, including using conductive fillers to improve conductivity and cycling stability and enhancing structural integrity via cross-linking to augment mechanical durability [35–37]. Also, the integration of redox-active molecules, including diaminoanthraquinone, triphenylamine, phenazine, ferrocene, and aza-fused ring, into the molecular architecture of CMPs is an efficacious approach to augment their electrochemical properties, especially capacitance [38–42].

Heteroatom-rich POPs are a key class of materials that incorporate nitrogen, oxygen, sulfur, and phosphorus elements. The inclusion of heteroatoms significantly enhances the properties and functionality of CMPs, making them particularly valuable for applications in energy storage [43–45]. Developing polymer networks functionalized with nitrogen heterocycles is essential for improving electrochemical properties, including enhanced conductivity, wettability, and increased pseudocapacitance [46,47]. Pyridine is a heterocyclic aromatic molecule with the molecular formula C_5H_5N [48]. Pyridine-derived compounds enhance charge transfer, thermal and electrochemical stability, and electrode conductivity, rendering them advantageous electroactive materials for energy storage and conversion systems [49–51]. Anthraquinones (AQ) is a category of chemical compounds distinguished by a three-ring structure originating from anthracene, featuring two ketone groups at positions 9 and 10 of the anthracene framework, with a general chemical formula of $C_{14}H_8O_2$ [52]. AQ derivatives are multifaceted molecules with considerable potential for various applications, including commercial uses in dyes and pigments and innovative technologies in energy storage and healthcare [53,54].

To our knowledge, there have been no documented studies or examinations about the utilization of CMP skeletons, which include 1,4-bis(2,6-bis(4-bromophenyl)pyridin-4-yl)benzene (BTPP-4Br) and redox-active 2,6-dibromoanthracene-9,10-dione (AQ-2Br). This study successfully employed Suzuki-Miyaura coupling polymerization to synthesize two redox-active pyridine and anthraquinone CMPs (BTPP-Ph-AQ and BTPP-BPh-AQ CMPs) for energy storage applications. The BTPP-Ph-AQ CMP was synthesized via the reaction of (BTPP-4Br) (Scheme S1), 1,4-phenylenediboronic acid (Ph-2BO), and (AQ-2Br) (Scheme S2), in DMF, while the BTPP-BPh-AQ CMP was prepared using (BTPP-4Br), 1,1′-biphenyl-4,4′-boronic acid (BPh-2BO), and (AQ-2Br) (Schemes S3, S4, and 1). It is well established that a material's structure critically influences its electrochemical performance. In this context, anthraquinone emerges as an ideal building block due to its excellent redox properties, high specific capacity, extended conjugation, and superior planarity, making it highly effective for enhancing electrochemical characteristics [55,56]. Biphenyl, consisting of two benzene rings connected by a single bond, is a non-planar, high molecular-weight molecule [57]. Prior data shows that BTPP-Ph-AQ CMP has a higher surface area of 254 $m^2\ g^{-1}$, excellent thermal stability, a specific capacity of 632.76 F g^{-1} at 0.5 A g^{-1}, and remarkable cycling stability, retaining 84.29 % of its original capacitance after 10,000 charge-discharge cycles. BTPP-Ph-AQ CMP can also be used to make symmetric two- and three-electrode capacitors for charge energy storage.

2. Experimental

2.1. Materials

Terephthalaldehyde (98 %) and 4-bromoacetophenone (98 %) were obtained from Alfa Aesar, while 1,4-benzenediboronic acid (96 %) was sourced from Thermo Scientific. Additional reagents and materials used to synthesize polymers are detailed in the Supporting Information (Section S1. Materials).

2.2. Preparation of BTPP-Ph-AQ CMP

Scheme S3 describes the Suzuki coupling synthesis of BTPP-Ph-AQ CMP. In a 50 mL two-neck flask, 1,4-bis(2,6-bis(4-bromophenyl)pyridin-4-yl)benzene (150 mg, 0.176 mmol), 1,4-phenylenediboronic acid (116.69 mg, 0.706 mmol), 2,6-dibromoanthracene-9,10-dione (128.75 mg, 0.352 mmol), and $Pd(PPh_3)_4$ (21 mg, 0.018 mmol). The reaction mixture received 25 mL of DMF and 550 mg of potassium carbonate in 5 mL of aqueous solution. The tube was heated for 72 h at 130 °C. The reaction mixture was centrifuged and washed three times with THF until

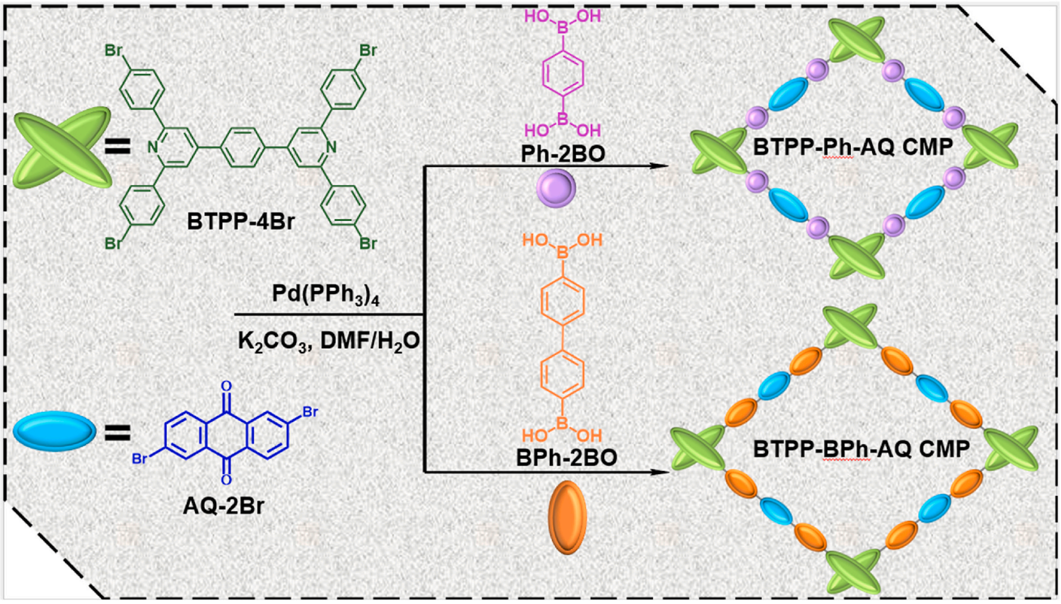

Scheme 1. Design and synthesis manner of BTPP-Ph-AQ and BTPP-BPh-AQ CMPs.

colorless after cooling to 25 °C. The method produced 66.02 % BTPP-Ph-AQ as a pale green solid.

2.3. Preparation of BTPP-BPh-AQ CMP

Scheme S4 describes the Suzuki coupling synthesis of BTPP-BPh-AQ CMP. In a 50 mL two-neck flask, 1,4-bis(2,6-bis(4-bromophenyl)pyridin-4-yl)benzene (150 mg, 0.176 mmol), 1,1′-biphenyl-4,4′-boronic acid (170.73 mg, 0.706 mmol), 2,6-dibromoanthracene-9,10-dione (128.75 mg, 0.352 mmol), and $Pd(PPh_3)_4$ (21 mg, 0.018 mmol). The reaction mixture received 25 mL of DMF and 550 mg of potassium carbonate in 5 mL of aqueous solution. The tube was heated for 72 h at 130 °C. The reaction mixture was centrifuged and washed three times with THF until colorless after cooling to 25 °C. The method produced 57.6 % BTPP-BPh-AQ CMP as a pale green solid.

3. Results and discussion

3.1. The production and characterization of materials

We successfully synthesized BTPP-Ph-AQ and BTPP-BPh-AQ CMPs utilizing the precursors BTPP-4Br (Scheme S1 and Fig. S1–3) and AQ-2Br (Scheme S2), which were produced with high yields according to recorded protocols in the literature [58,59], as detailed in the respective

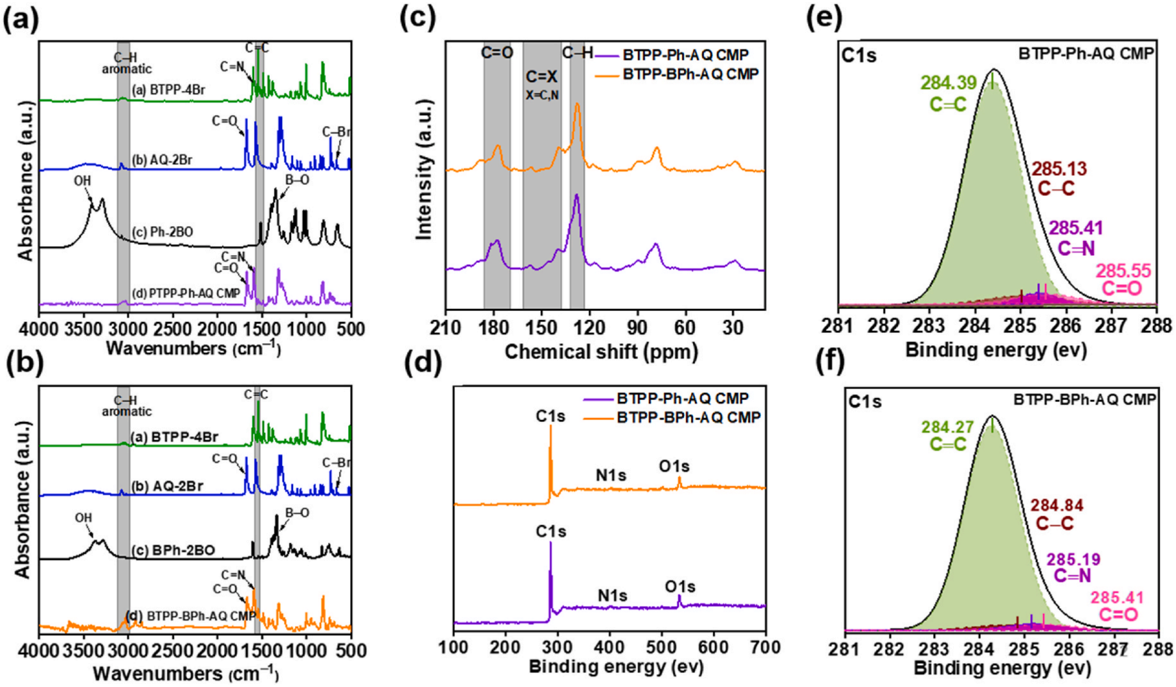

Fig. 1. (a,b) FT-IR spectra of (a) BTPP-Ph-AQ CMP and its monomers. (b) BTPP-BPh-AQ CMP and its monomers. (c) Solid-state ^{13}C NMR spectra of BTPP-Ph-AQ and BTPP-BPh-AQ CMPs. (d) XPS survey spectra of BTPP-Ph-AQ and BTPP-BPh-AQ CMPs. (e,f) XPS spectra of the (e) C1s for the BTPP-Ph-AQ CMP and (f) C1s for the BTPP-BPh-AQ CMP.

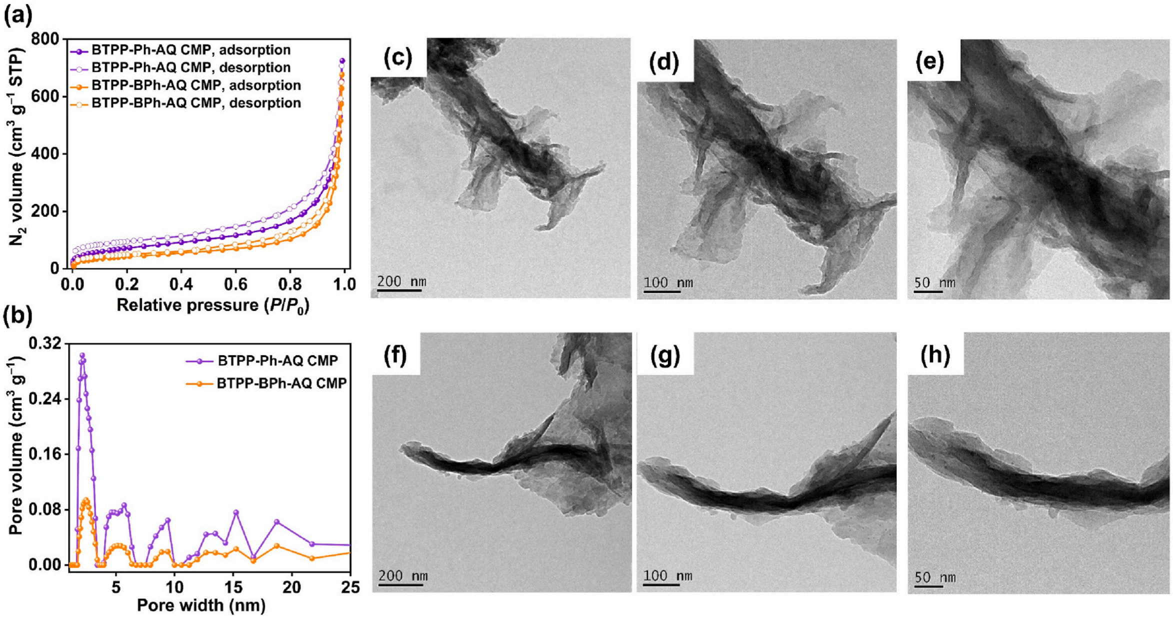

Fig. 2. (a) Nitrogen adsorption and desorption isotherms at 77K and (b) Distribution curves for pore size in CMPs. (c–h) HR-TEM photos of (c–e) BTPP-Ph-AQ CMP and (f–h) BTPP-BPh-AQ CMP.

synthetic pathways depicted in (Schemes 1, S3, and, S4). BTPP-Ph-AQ CMP (Schemes 1 and S3) was obtained as non-soluble pale green solids via the incorporation of Ph-2BO and AQ-2Br with BTPP-4Br, whereas combining BPh-2BO and AQ-2Br with BTPP-4Br to give non-soluble pale green solids of BTPP-BPh-AQ CMP (Schemes 1 and S4). The resultant CMPs demonstrate very limited solubility in common solvents including alcohols, acetone, dimethylformamide (DMF), and tetrahydrofuran (THF), hence affirming their robust crosslinking. Following thorough purification, inductively coupled plasma atomic emission spectroscopy (ICP-AES) indicates limited palladium impurities (0.02–0.03 mol%) in the resulting BTPP-Ph-AQ and BTPP-BPh-AQ CMPs.

The chemical composition and thermal characteristics of the produced CMPs were verified using multiple analyses, including infrared (FTIR), solid-state ^{13}C NMR (SS NMR), X-ray photoelectron spectroscopy (XPS), and thermogravimetric analysis (TGA) examinations. The FTIR profiles of BTPP-Ph-AQ and BTPP-BPh-AQ CMPs exhibit absorption signals at 3039 and 3034 cm^{-1} for C–H aromatic bonds, 1674 and 1671 cm^{-1} for C=O, 1596 and 1594 cm^{-1} for C=N, and 1546 and 1545 cm^{-1} for C=C vibration (Fig. 1a and b). The total lack of B–O and OH stretching vibration peaks in both CMPs in comparison to their progenitors, Ph-2BO (1350 cm^{-1}) and BPh-2BO (1344 cm^{-1}), accompanied by the absence of the C–Br bond absorbance peak at 663 cm^{-1} in the BTPP-4Br head monomer signifies the successful creation complete coupling between the monomers, leading to the desired polymers. Moreover, SS NMR of BTPP-Ph-AQ and BTPP-BPh-AQ CMPs presented three principal resonance areas at 186–172, 160–142, and 139–122 ppm, corresponding to the carbonyl C=O, aromatic C = X (X = C, N), and aryl C–H carbon nuclei, respectively (Fig. 1c). The prior results provide additional confirmation that the monomer molecules were polymerized entirely. XPS is employed to ascertain the types and quantities of elements in a sample, investigate the elements' oxidation states and chemical surroundings, and examine the chemical bonding and interactions at the material's surface. Fig. 1d illustrates the O 1s, N 1s, and C 1s orbitals, which exhibit three prominent peaks at 533, 398, and 286 eV for the BTPP-Ph-AQ CMP, and at 534, 400, and 286 eV for the BTPP-BPh-AQ CMP. As a result, the lack of additional components in the XPS analysis suggests that no unwanted substances were present throughout the synthesis of our CMPs. To further understand the C species identified in our CMPs, we fitted the experimental XPS data to the C 1s orbital. As shown in Fig. 1e and Table S1, the subdivision of C 1s orbital of the BTPP-Ph-AQ CMP into four peaks: 284.39 eV for C=C bonds, 285.13 for C–C bonds, 285.41 for C=N bonds, and 285.55 for C=O bonds. The subdivision of C 1s orbital of the BTPP-BPh-AQ CMP onto four peaks: 284.27 eV for C=C bonds, 284.84 for C–C bonds, 285.19 for C=N bonds, and 285.41 for C=O bonds (Fig. 1f and Table S1). The BTPP-Ph-AQ CMP exhibits bond contents of 87.09 %, 5.15 %, 3.42 %, and 4.33 %, corresponding to C=C, C–C, C=N, and C=O, respectively, while the BTPP-BPh-AQ CMP shows values of 89.73 %, 4.15 %, 2.68 %, and 3.45 %, respectively (Table S2). Following sensitivity factor correction, the elemental ratios in the CMPs were obtained by analyzing the peak areas of each component in the XPS survey spectrum. The elemental ratios of BTPP-Ph-AQ and BTPP-BPh-AQ CMPs were experimentally determined by analyzing the peak areas of each element in the XPS survey spectra, adjusted using sensitivity factors. The results, summarized in Table S3, show a strong correlation with the theoretical elemental ratios derived from the chemical structures of the respective CMPs, as presented in Table S4. The thermal stabilities of our synthesized polymeric frameworks were examined using TGA. This measurement was assessed under a nitrogen flow from 100 °C to 800 °C. TGA of the BTPP-Ph-AQ and BTPP-BPh-AQ CMPs indicated elevated thermal decomposition temperatures at 10 % weight loss (638.43 °C and 634.62 °C, respectively), along with significant char yields of 78.9 % and 75.02 % (Fig. S4 and Table S5). The exceptional thermal stability of these CMPs probably arises from the thermal stability of pyridine moieties and the planarity of anthraquinone units, which enhance π-stacking interactions inside the CMP layers.

3.2. *Porosity and morphology*

Gas adsorption and desorption analyzes utilizing nitrogen as the adsorbate at 77 K are a conventional technique for evaluating the porosity of materials, particularly for porous substances such as conjugated microporous polymers (CMPs) (Fig. 2a and b). Following that, utilizing the Brunauer-Emmett-Teller (BET) theory on gas adsorption data to provide a quantitative comprehension of the surface area and porosity attributes of our CMPs. The N$_2$ sorption isotherms at 77 K for BTPP-Ph-AQ CMP and BTPP-BPh-AQ CMP exhibit Type IV behavior with

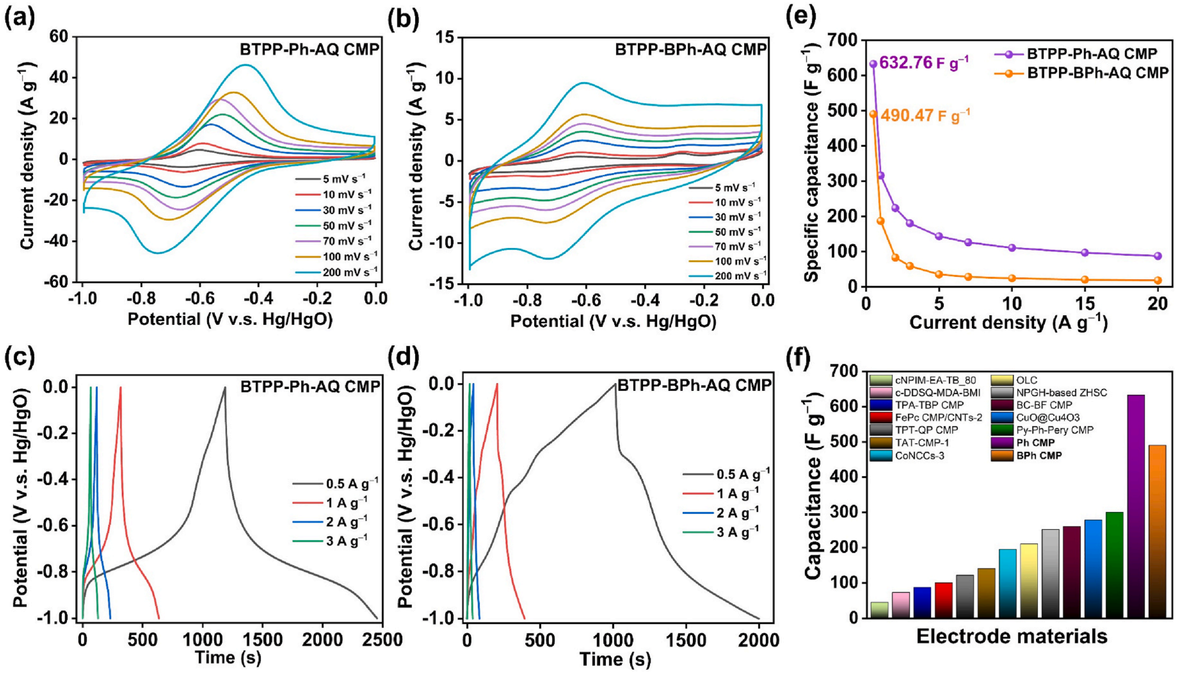

Fig. 3. (a,b) CV curves and (c,d) GCD curves of (a,c) the BTPP-Ph-AQ and (b,d) BTPP-BPh-AQ CMPs, tested at different scans. (e) Determined specific capacitances of the BTPP-Ph-AQ and BTPP-BPh-AQ CMPs, tested at different current densities. (f) Specific capacitances of BTPP-Ph-AQ and BTPP-BPh-AQ CMPs compared to earlier reported redox-active CMPs.

H3- type hysteresis loops, indicating mesoporous structures with slit- or wedge-shaped pores. The minimal adsorption at low relative pressures ($P/P_0 < 0.1$) suggests limited microporosity, while the increased uptake at higher relative pressures ($P/P_0 > 0.9$) is attributed to capillary condensation in mesopores (Fig. 2a). The presence of hysteresis loops between the adsorption and desorption branches further confirms the mesoporous character of both CMP. These characteristics align with the amorphous and possibly aggregated nature of the CMP networks. We also calculated the pore volumes and BET specific surface areas of the synthetic CMPs using their curves; for the BTPP-Ph-AQ CMP, these were 0.30 cm^3 g^{-1} and 254 m^2 g^{-1}, respectively; and for the BTPP-BPh-AQ CMP, these were 0.09 cm^3 g^{-1} and 169 m^2 g^{-1}, respectively. Fig. 2b and Table S6 show the results of using nonlocal density functional theory (NL-DFT) to predict the pore dimensions of BTPP-Ph-AQ CMP and BTPP-BPh-AQ CMP. According to Fig. 2b and Table S6, BTPP-Ph-AQ CMP has a microporous structure with pore dimensions ranging from 1.65 to 3.41 nm and a few mesopores measuring 3.77–6.7 nm. Microporous BTPP-BPh-AQ CMP has pores ranging from 1.72 to 3.59 nm and a small number of mesopores from 3.97 to 6.72 nm. In agreement with the isotherm curves, the majority of the measured pore sizes fell into the microporous and mesoporous categories. Reports indicate that polymers maintaining a planar structure frequently have expanded surface areas [41]. Consequently, the results align with the planarity of the CMPs; the BTPP-Ph-AQ CMP demonstrated more excellent planarity, resulting in high BET surface area, whereas the BTPP-BPh-AQ CMP demonstrated reduced planarity, causing reduced BET surface area.

The structural morphologies of our new polymers have been examined using both field emission scanning electron microscopy (FE-SEM) and high-resolution transmission electron microscopy (HR-TEM) research. The TEM pictures of both BTPP-Ph-AQ and BTPP-BPh-AQ CMPs reveal an ordered nanorod morphology, with nanorod lengths extending to several micrometers (Fig. 2c–h). We ascribe the rod-like shape of our novel CMPs to the planarity of their monomers, AQ, and Ph units, as well as the hydrogen bonding between the hydrogen and oxygen atoms, or perhaps between the hydrogen and nitrogen atoms. Field-effect SEM affirms the nanorod morphology of the BTPP-Ph-AQ and BTPP-BPh-AQ CMPs (Fig. S5a–d). Atoms of oxygen, nitrogen, and carbon were found to be evenly distributed across the polymer framework's surface, according to elemental mapping produced using energy dispersive X-ray spectroscopy (EDS) (Figs. S5e–g and h–j).

3.3. Electrochemical properties

Our BTPP-Ph-AQ and BTPP-BPh-AQ CMPs display redox-active properties, remarkable thermal stability, extensive surface areas, rod-like structures, and hierarchical micro- and mesopore architectures, making them talent supercapacitor materials. We examined the electrochemical behavior of our novel CMPs using cyclic voltammetry (CV) and galvanostatic charge/discharge (GCD) in a setup with three electrodes submerged in aqueous KOH (3 M) as electrolyte. Thus, we initially evaluated the electrical and electrochemical properties of these CMPs in a 3 M KOH aqueous electrolyte with a three-electrode configuration, employing platinum wire, Hg/HgO and glassy carbon as the counter electrode, reference electrode, and working electrode, respectively. We documented the CV curves of asymmetric supercapacitors utilizing BTPP-Ph-AQ and BTPP-BPh-AQ CMPs within the −1.0 to 0 V potential range at various scan rates ranging from 5 to 200 mV s^{-1} (Fig. 3a and b) [60]. Fig. 3a and b illustrate the peak potentials for the oxidation and reduction of BTPP-Ph-AQ CMP were measured at −0.0.61 and −0.66 V, respectively, at a scan rate of 5 mVs^{-1}; for BTPP-BPh-AQ CMP, the corresponding values were −0.64 and −0.74 V. In comparison to the BTPP-BPh-AQ CMP, the BTPP-Ph-AQ CMP offers a greater current density. The rectangular shapes seen in the CV curves of these CMPs point to EDLC as the main source of capacitive response, with almost little pseudocapacitance owing to the electron-rich phenyl rings, oxygen, and nitrogen heteroatoms present [61–63]. Increasing the sweep rate from 5 to 200 mV s^{-1} increased current density while retaining the CV curve form, exhibiting quick kinetics and rate capabilities [64]. Our CMPs' short oxidation-reduction band intervals indicate fast electron transport across AQ and BTPP. All previous observations supported the redox process's quasi-reversibility. We examined the validity of galvanostatic charging-discharging to gain a deeper understanding of the electrochemical-specific capacitances of our CMPs. The GCD scans of BTPP-Ph-AQ and BTPP-BPh-AQ CMPs were conducted at various current

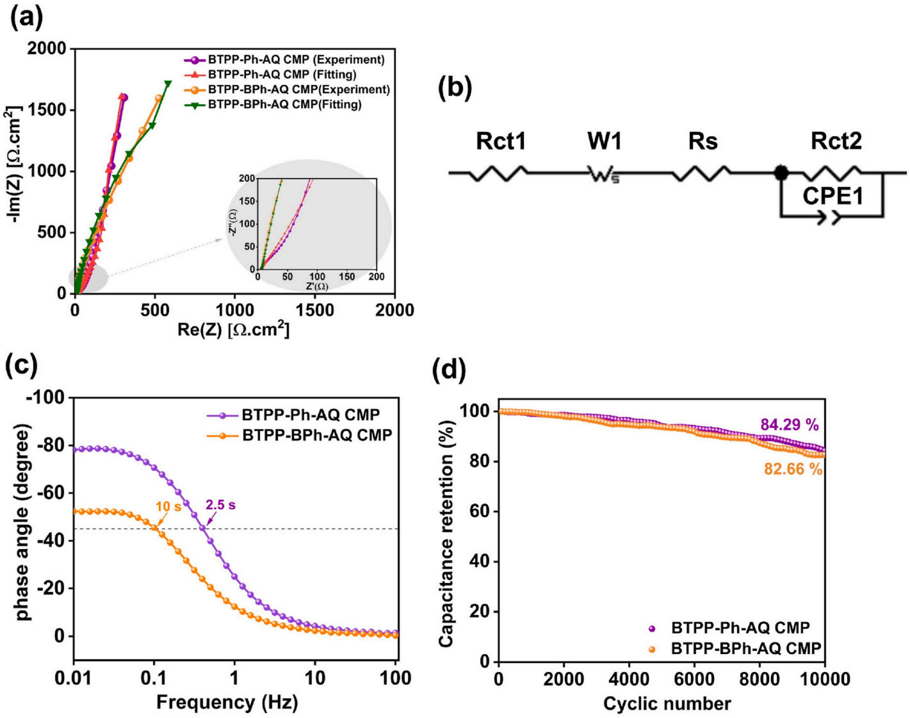

Fig. 4. (a) The ortho-normed Nyquist plot and the fitted plot that corresponded, (b) equivalent circuit, (c) Bode plots, and (d) cycling efficiency of the BTPP-Ph-AQ and BTPP-BPh-AQ CMPs. The stability is tested at a current density of 10 A g^{-1}.

densities ranging from 0.5 to 20 A g^{-1} (Fig. 3c,d and Fig. S6). The GCD plateaus of BTPP-Ph-AQ exhibit triangular shapes with pronounced bending, validating its pseudocapacitance and electric double-layer capacitance characteristics [65]. The BTPP-BPh-AQ CMP GCD curve is slightly curved and triangular, suggesting that the higher efficacy is due to EDLC. This behavior matches CV scan results, which are due to the enhanced planarity of the phenyl ring and the redox AQ unit derived from BTPP-Ph-AQ CMP. Furthermore, the abundance of redox sites in both CMPs situated at the pyridine and anthraquinone moieties presents a significant potential for pseudocapacitance [66]. Fig. 3c and d shows that the BTPP-Ph-AQ CMP had a longer discharging time than the BTPP-BPh-AQ, indicating a higher capacitance. We used Eq. (S1) to calculate the specific capacitances from GCD curves (Fig. 3e). At current densities of 0.5, 1.0, 2.0, 3.0, 5.0, 7.0, 10.0, 15.0, and 20.0 A g^{-1}, the specific capacitances for the BTPP-Ph-AQ CMP were 632.76, 316.40, 223.78, 180.44, 143.83, 126.35, 110.90, 96.83, and 87.50 F g^{-1}, whereas for the BTPP-BPh-AQ CMP were 490.47, 187.26, 83.16, 59.22, 35.75, 28.70, 24.50, 20.55 and 18.60 F g^{-1}, respectively. The slightly higher capacitances of BTPP-Ph-AQ compared to BTPP-BPh-AQ are apparently ascribed to the phenyl group demonstrating superior planarity compared to the biphenyl system, which enhances aromaticity and thus improves electron transport characteristics [41]. Additionally, high molecular weight of BTPP-BPh-AQ compared to BTPP-Ph-AQ can induce entanglement and disordered packing, hence restricting ion mobility and diminishing conductivity. Furthermore, a reduced number of active sites diminishes the faradaic input, which is crucial to the operation of pseudocapacitors. The reduced number of active sites limits the polymer's capacity to hold charge per unit of mass or surface, resulting in diminished energy storage capacity. Furthermore, the drop in capacitance at elevated current densities may be ascribed to a variety of factors, including limitations in ion transport, increased polarization, resistive losses, side reactions, and potential electrode material damage. In overall, our research shown that the superior electrochemical performance of BTPP-Ph-AQ and BTPP-BPh-AQ CMPs stems from their large surface areas, substantial pore volumes, and the integration of redox-active AQ units within the polymer framework, which significantly enhances charge storage capacity and redox behavior. BTPP-Ph-AQ and BTPP-BPh-AQ CMPs exhibit specific capacitance values that exceed those reported for similar redox-active materials (Fig. 3f and Table S7) [5,41,67–76]. Our synthesized CMPs provide various advantages over inorganic Faradaic materials, including increased tunability, lighter and more flexible designs, improved chemical stability, cost-effectiveness, scalability, and environmental sustainability. Their unique combination of organic and conjugated nature improves performance in energy storage and conversion systems, providing greater design flexibility and stability in practical applications than typical inorganic materials.

Fig. S7a and b depict the BTPP-Ph-AQ CMP redox-dependent mechanism. In the AQ redox interaction pathway, two electrons are reduced to generate the AQ^{2-} anion (Fig. S7a) [77]. Fig. S7b shows that AQ structures were reduced during discharge and AQ^{2-} oxidized during charge. The redox-dependent process involving BTPP-BPh-AQ CMP is illustrated in Fig. S8a and b. The redox mechanism is validated using the cyclic voltammetry measurements of BTPP-4Br and AQ-2Br (Fig. S9a and b). Cyclic voltammetry experiments indicate that AQ is the primary redox-active component, whereas BTPP does not directly engage in redox processes but can affect the electronic characteristics of the entire CMP. BTPP may indirectly influence the redox behavior of AQ by altering its surrounding electronic environment, despite BTPP exhibiting no redox activity independently. The CV curves (Fig. 3a and b) show a single pair of combination events between BTPP and AQ (−0.61 and −0.66 V in BTPP-Ph-CMP and −0.64 and −0.74 V in BTPP-BPh-CMP). Furthermore, because the BTPP-Ph-AQ and BTPP-BPh-AQ CMPs have a medium surface area, a redox-active technique rather than a double-layer strategy is used to regulate their capacity.

Electrochemical impedance spectroscopy (EIS) serves as a standard technique for investigating charge storage kinetics. The ortho-normed Nyquist plots (−Im(Z) vs. Re(Z)) of BTPP-Ph-AQ CMP and BTPP-BPh-AQ CMP electrodes are presented in Fig. 4a. The measurements were conducted in 3 M KOH at 25 °C over a frequency range of 100 kHz to 0.01 Hz, using 10 points per decade, an AC amplitude of 5 mV, and a frequency sweep from high to low. The CMP electrodes exhibited

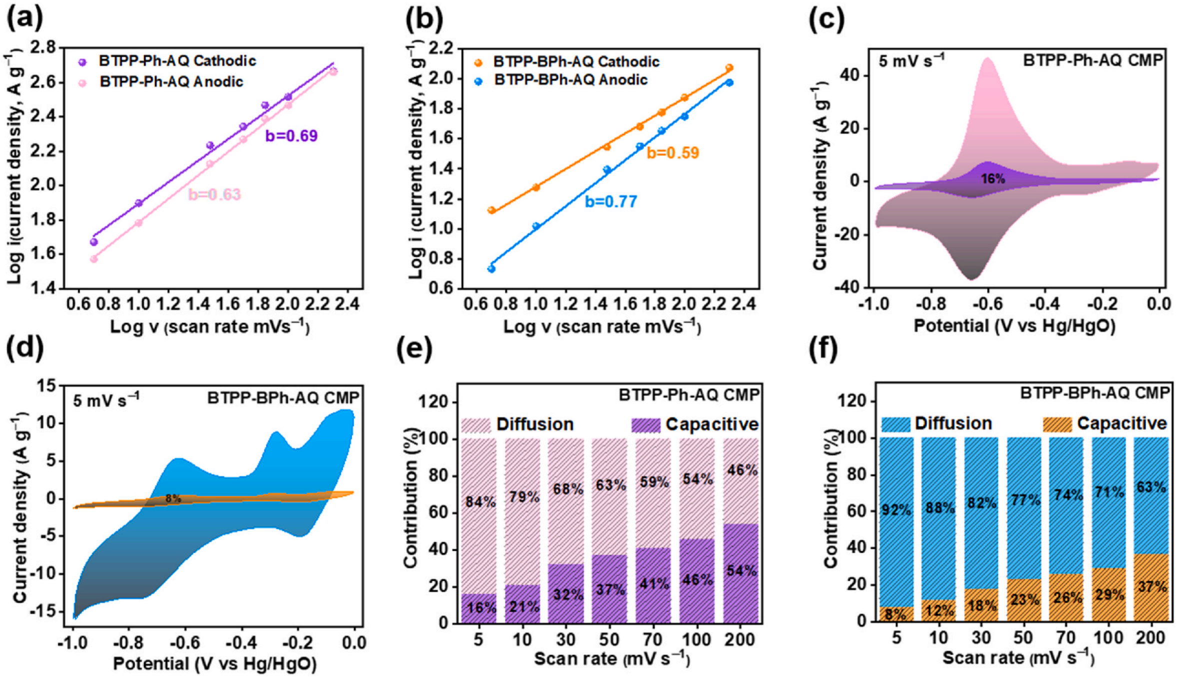

Fig. 5. (a,b) log(i) against log(v) plots and (c, d) capacitive and diffusion contributions tested at 5 mV s^{-1} of (a,c) BTPP-Ph-AQ and (b,d) BTPP-BPh-AQ CMPs. (e,f) Capacitive and diffusion-controlled storage for charges of (e) BTPP-Ph-AQ and (f) BTPP-BPh-AQ CMPs at different scans.

minimal charge transfer resistance and excellent conductivity, as evidenced by the small semicircle in the high-frequency region [78]. A diffusion-controlled process manifests as a nearly vertical straight line in the lower frequencies zone, indicating a decreased ionic diffused resistance within the conducting electrode and the electrolytic solution [79]. At elevated frequencies, the pattern is linked to the relaxation of faradaic redox capacitors with a redox-active layer (Fig. 4a). AQ/AQ^{2-}'s pseudo-redox reaction causes capacitors to relax. By examining the interception on the Z$'$ axis, we determined the intrinsic ohmic resistance (R_s), which indicates the conductivity of the electrodes. The BTPP-Ph-AQ CMP electrode showed improved ion accessibility and reduced charge transfer resistance, as reflected by its lower R_s value of 0.66 Ω compared to 1.49 Ω for the BTPP-BPh-AQ CMP (Fig. 4a). R_s represents electrolyte resistance, R_{ct} represents charge transfer resistance at the electrode interface, and W and CPE represent Warburg impedance and constant phase element, respectively, in a circuit model (Fig. 4b) that fit EIS results. Table S8 displays R_s and R_{ct1} values of 0.66 and 4.08 Ω for the BTPP-Ph-AQ CMP, and 1.49 and 5.22 Ω for the BTPP-BPh-AQ CMP. The R_{ct} value reduced from BTPP-Ph-AQ to BTPP-BPh-AQ CMP because the phenyl ring in BTPP-Ph-AQ CMP is more planar and lower molecular weight than the biphenyl group in BTPP-BPh-AQ CMP. The BTPP-Ph-AQ CMP-based electrode exhibits superior pseudocapacitance compared to the BTPP-BPh-AQ electrode, attributable to its reduced R_{ct2} value [80]. The Bode graphs (Fig. 4c) show that the BTPP-Ph-AQ and BTPP-BPh-AQ CMPs had relaxation time constants of 2.5 and 10 s, respectively, indicating their significant diffusion and transport capabilities. The BTPP-Ph-AQ CMP-based electrode demonstrated elevated conductivity and capacitance, supporting previous findings. As shown in Fig. 4d, we have tested our materials' capacitance retention by subjecting them to 10,000 GCD cycles at 10 A g^{-1}. Notably, the CMPs that were produced, BTPP-Ph-AQ CMP (84.29 %) and BTPP-BPh-AQ CMP (82.66 %), exhibit remarkable cyclic stability. According to all the results reported earlier, the specific capacitance and lifespan of the associated supercapacitor were significantly increased when redox-active AQ and a planar phenyl ring were integrated into the CMP backbone. At room temperature, the four-probe techniques were also used to assess the electron conductivity of CMPs. BTPP-Ph-AQ CMP exhibits a conductivity of 4.26 S/cm, surpassing the conductivity of BTPP-BPh-AQ CMP (1.07 × 10^{-2} S/cm) and surpassing the conductivity of a multitude of other organic materials that are comparable (Table S9). Following a 4-h immersion in 1M and 3M KOH, we measured the BTPP-Ph-AQ and BTPP-BPh-AQ CMPs by FT-IR (Fig. S10). Functional groups associated with redox activity, such as C=O, show no notable changes or the absence of intensity, and peaks that include conjugated skeletons, like C=C stretching in aromatic rings, remain intact according to the analysis. The spectra obtained before and after immersing in KOH are nearly comparable, confirming the stability of the CMP network structure.

To elucidate the capacitive contribution of BTPP-Ph-AQ and BTPP-BPh-AQ CMPs, we analyzed the correlation between electrical current (i) and scan rate (v) utilizing the subsequent power law equation (Eq. (1)) [81].

$$i = av^b \tag{1}$$

The value of "b" was estimated by calculating the slope of a log(i) vs log(v) plot, with "a" standing for a constant value. The BTPP-Ph-AQ CMP showed anodic and cathodic peaks with calculated b values of 0.63 and 0.69, respectively, (Fig. 5a). In contrast, the BTPP-BPh-AQ CMP showed anodic and cathodic peaks with calculated b values of 0.77 and 0.59, respectively, (Fig. 5b). The findings and interpretations proved that these CMPs could store energy using a combination of capacitive and diffusion-controlled mechanisms [82]. The enhanced capacitance of BTPP-Ph-AQ CMP is proved by its extra capacitive contribution relative to BTPP-BPh-AQ CMP. Eq. (2) calculates capacitive contribution to total capacity [81].

$$i(V) = k_1 v + k_2 v^{1/2} \tag{2}$$

Regarding a constant potential V, the total current is denoted as i(V), with $k_1 v$ and $k_2 v^{1/2}$ representing the currents generated by the diffusion-controlled mechanism and capacitive effects, respectively. According to Fig. 5c and d, the BTPP-Ph-AQ and BTPP-BPh-AQ CMPS were found to contribute 16 % and 8 % of the total capacitance, respectively, when measured at a rate of 5 mV s^{-1}. At a scan rate of 200 mV s^{-1}, the capacitive contribution for the BTPP-Ph-AQ CMP climbed to 54 %

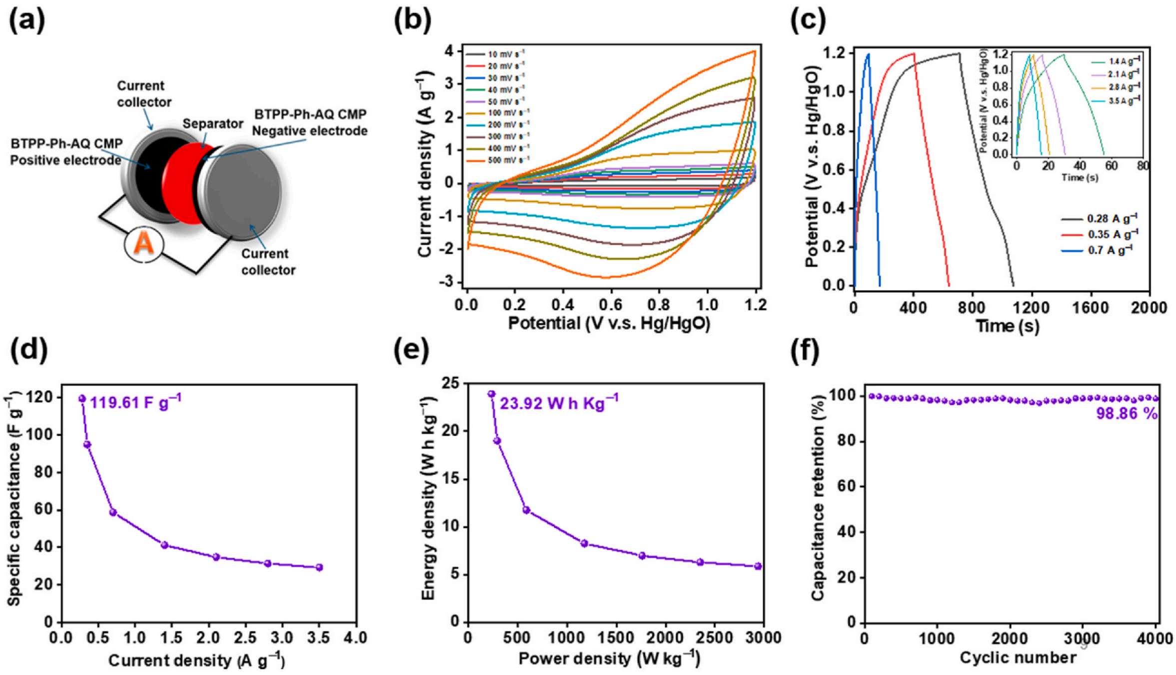

Fig. 6. (a) Graphic design of the BTPP-Ph-AQ CMP-based SC device. (b) CV curves, (c) GCD curves, (d) Specific capacitances, (e) Ragone plots, and (f) cycling efficiency tested at a current density of 3.5 A g^{-1} of the BTPP-Ph-AQ CMP-based SC device.

(Fig. 5e), while for the BTPP-BPh-AQ CMP it grew to 37 % (Fig. 5f). The reason for this is that when scan speeds increase, ion diffusion into the CMP's network becomes faster.

We developed a symmetric supercapacitor (SC) device utilizing a two-electrode configuration to investigate the feasibility of BTPP-Ph-AQ CMP in practical supercapacitor applications. Two flexible BTPP-Ph-AQ CMP-based electrodes coated on carbon sheets were separated by a piece of filter paper, and the electrolyte was a 3 M KOH solution (Fig. 6a). Fig. 6b shows that when the scan speeds ranged from 10 to 500 mV s^{-1}, and the potential range was from +0.0 to +1.2 V, the quasi-reversible patterns in the CV recordings demonstrated quick electrolyte diffusion into the electrode layer. Throughout the whole sweep, these profiles remained remarkably unchanged [83]. Displayed in Fig. 6c are the GCD graphs for current densities ranging from 0.28 A g^{-1} to 3.5 A g^{-1} of the BTPP-Ph-AQ CMP-based SC system. Based on the mass of the individual electrodes, the BTPP-Ph-AQ CMP tethered SC is assumed to have particular capacitances at various current densities, as shown in Fig. 6d. At various current densities (0.28, 0.35, 0.7, 1.4, 2.1, 2.8, and 3.5 A g^{-1}), the specific capacitances of the SC were 119.61, 95, 58.77, 41.20, 34.83, 31.46, and 29.29 F g^{-1}. Our BTPP-Ph-AQ CMP-tethered SC showed excellent capacitance maintenance even at high current densities, according to these results. These capacitance values are also higher than those of symmetric SC devices and SC devices with different electrodes that are assessed using the same redox-active materials [84–88] (27–87 F g^{-1}). The Ragone plot (Fig. 6e) shows that the BTPP-Ph-AQ CMP-based SC device reached 23.92 Wh kg^{-1} energy density, and 234.97 W kg^{-1} power density. Although the power density was increased to 2937.06 W kg^{-1}, the energy density of the BTPP-Ph-AQ CMP-based SC device was 5.86 Wh kg^{-1} and 1.2 V. These values are higher than those of symmetric SC devices and supercapacitors that have been disclosed before, which use similar redox-active materials [69,89–92]. Fig. 6f clarifies the BTPP-Ph-AQ CMP-based supercapacitor's 98.86 % capacitance retention after 4000 cycles of GCD at 3.5 A g^{-1}, demonstrating excellent cycle durability and rate efficacy.

4. Conclusions

In conclusion, we effectively synthesized two types of CMPs utilizing pyridine and anthraquinone units with favorable yields via one-step Suzuki coupling polymerization, as confirmed by FTIR and solid-state NMR spectroscopy. The planarity and nitrogen concentration of monomers influenced BET surface area of CMPs. For planar monomers, the BTPP-Ph-AQ CMP formed from the most planar monomers had a much greater BET surface area of 254 m^2 g^{-1} compared to the BTPP-BPh-AQ created from less planar and higher molecular weight monomers. A conjugated structure with redox-active anthraquinone and pyridine units allowed the BTPP-Ph-AQ CMP to have the highest electron conductivity (4.26 Siemen/cm) and specific capacitance (632.76 F g^{-1} at 0.5 A g^{-1}). Capacitance measured at 119.61 F g^{-1}, and efficient energy density 23.92 Wh kg^{-1} at 234.97 W kg^{-1} and 1.2 V in the two-electrode symmetric supercapacitor system was recorded by BTPP-Ph-AQ CMP. Such study highlights the significance of monomer planarity and nitrogen content in the resulting CMPs. Furthermore, CMPs with redox-active groups may be ideal for use in energy storage devices.

CRediT authorship contribution statement

Shimaa Abdelnaser: Writing – original draft, Methodology, Investigation, Formal analysis, Data curation. **Shiao-Wei Kuo:** Supervision, Resources, Funding acquisition. **Ahmed F.M. EL-Mahdy:** Writing – review & editing, Writing – original draft, Supervision, Software, Resources, Project administration, Funding acquisition, Formal analysis, Data curation.

Declaration of competing interest

The authors declare that they have no known competing financial interests or personal relationships that could have appeared to influence the work reported in this paper.

Acknowledgements

This study was supported financially by the National Science and Technology Council, Taiwan, under contract NSTC 112-2221-E-110-005-MY3 and 113-2218-E-110-004-.

Appendix A. Supplementary data

Supplementary data to this article can be found online at https://doi.org/10.1016/j.jpowsour.2025.238225.

Data availability

Data will be made available on request.

References

[1] S. Sikiru, T.L. Oladosu, T.I. Amosa, J.O. Olutoki, M.N.M. Ansari, K.J. Abioye, Z. U. Rehman, H. Soleimani, Hydrogen-powered horizons: transformative technologies in clean energy generation, distribution, and storage for sustainable innovation, Int. J. Hydrogen Energy 56 (2024) 1152–1182, https://doi.org/10.1016/j.ijhydene.2023.12.186.

[2] S.R. Khatibi, M.M. Lakeh, S.M. Karimi, M. Kermani, S.A. Motevalian, Catalyzing healthier air: the impact of escalating fossil fuel prices on air quality and public health and the need for transition to clean fuels, Biofuel Res. J. 42 (2024) 2099–2104, https://doi.org/10.18331/BRJ2024.11.2.4.

[3] Z.Q.S. Nwokediegwu, K.I. Ibekwe, V.I. Ilojianya, E.A. Etukudoh, O.B. Ayorinde, C. Author, Renewable energy technologies in engineering: a review of current developments and future prospects, Eng. Sci. Technol. J. 5 (2024) 367–384, https://doi.org/10.51594/estj/v5i2.800.

[4] K.Y. Lin, A.F.M. EL-Mahdy, Covalent triazine frameworks based on triphenylpyridine building block for high-performance supercapacitor and selective CO2 capture, Mater. Chem. Phys. 281 (2022) 125850, https://doi.org/10.1016/j.matchemphys.2022.125850.

[5] M. Ahmed, M.G. Kotp, T.H. Mansoure, R.H. Lee, S.W. Kuo, A.F.M. EL-Mahdy, Ultrastable carbazole-tethered conjugated microporous polymers for high-performance energy storage, Microporous Mesoporous Mater. 333 (2022) 111766, https://doi.org/10.1016/j.micromeso.2022.111766.

[6] T.A. Kumaravelu, R.R. Jayapalan, H.-W. Chang, A. Kandasami, L. Vayssieres, C.-L. Dong, Energy storage chemistry: atomic and electronic fundamental understanding insights for high-performance supercapacitors, Appl. Phys. Rev. 11 (2024) 031324, https://doi.org/10.1063/5.0203665.

[7] M. Pantrangi, E. Ashalley, M.K. Hadi, H. Xiao, Y. Zhang, W. Ahmed, N. Singh, A. Alam, U. Younis, F. Ran, P. Liang, Z. Wang, Flexible micro-supercapacitors: materials and architectures for smart integrated wearable and implantable devices, Energy Storage Mater. 73 (2024) 103791, https://doi.org/10.1016/j.ensm.2024.103791.

[8] T.-L. Yang, J.-Y. Chen, S.-W. Kuo, C.-T. Lo, A.F.M. EL-Mahdy, Hydroxyl-functionalized covalent organic frameworks as high-performance supercapacitors, Polymers 14 (2022) 3428, https://doi.org/10.3390/polym14163428. Basel.

[9] W. Lyu, C. Yan, Z. Chen, J. Chen, H. Zuo, L. Teng, H. Liu, L. Wang, Y. Liao, Spirobifluorene-based conjugated microporous polymer-grafted carbon nanotubes for efficient supercapacitive energy storage, ACS Appl. Energy Mater. 5 (2022) 3706–3714, https://doi.org/10.1021/acsaem.2c00151.

[10] K.K. Patel, T. Singhal, V. Pandey, T.P. Sumangala, M.S. Sreekanth, Evolution and recent developments of high performance electrode material for supercapacitors: a review, J. Energy Storage 44 (2021) 103366, https://doi.org/10.1016/j.est.2021.103366.

[11] A. Pramitha, Y. Raviprakash, Recent developments and viable approaches for high-performance supercapacitors using transition metal-based electrode materials, J. Energy Storage 49 (2022) 104120, https://doi.org/10.1016/j.est.2022.104120.

[12] T.A. Gaber, L.R. Ahmed, A.F.M. EL-Mahdy, Efficient faradaic supercapacitor energy storage using redox-active pyrene-and benzodithiophene-4, 8-dione-tethered conjugated microporous polymers, J. Mater. Chem. A 11 (2023) 19408–19417, https://doi.org/10.1039/d3ta03198e.

[13] E. Dhandapani, S. Thangarasu, S. Ramesh, K. Ramesh, R. Vasudevan, N. Duraisamy, Recent development and prospective of carbonaceous material, conducting polymer and their composite electrode materials for supercapacitor—A review, J. Energy Storage 52 (2022) 104937, https://doi.org/10.1016/j.est.2022.104937.

[14] L. Hao, X. Li, L. Zhi, Carbonaceous electrode materials for supercapacitors, Adv. Mater. 25 (2013) 3899–3904, https://doi.org/10.1002/adma.201301204.

[15] R. Liu, A. Zhou, X. Zhang, J. Mu, H. Che, Y. Wang, T.-T. Wang, Z. Zhang, Z. Kou, Fundamentals, advances and challenges of transition metal compounds-based supercapacitors, Chem. Eng. J. 412 (2021) 128611, https://doi.org/10.1016/j.cej.2021.128611.

[16] Y. Gao, L. Zhao, Review on recent advances in nanostructured transition-metal-sulfide-based electrode materials for cathode materials of asymmetric supercapacitors, Chem. Eng. J. 430 (2022) 132745, https://doi.org/10.1016/j.cej.2021.132745.

[17] G. Zhang, L. Deng, J. Liu, J. Zhang, J. Wang, W. Li, X. Li, Controllable intercalated polyaniline nanofibers highly enhancing the utilization of delaminated RuO_2 nanosheets for high-performance hybrid supercapacitors, Chemelectrochem 9 (2022) e202200039, https://doi.org/10.1002/celc.202200039.

[18] Y. Ma, X. Xie, W. Yang, Z. Yu, X. Sun, Y. Zhang, X. Yang, H. Kimura, C. Hou, Z. Guo, W. Du, Recent advances in transition metal oxides with different dimensions as electrodes for high-performance supercapacitors, Adv. Compos. Hybrid Mater. 4 (2021) 1–19, https://doi.org/10.1007/s42114-021-00358-2.

[19] S. Wang, C. Qu, J. Wen, C. Wang, X. Ma, Y. Yang, G. Huang, H. Sun, S. Xu, Progress of transition metal sulfides used as lithium-ion battery anodes, Mater. Chem. Front. 7 (2023) 2779–2808, https://doi.org/10.1039/d2qm01200f.

[20] D. Zhang, L. Miao, Z. Song, X. Zheng, Y. Lv, L. Gan, M. Liu, Electrolyte additive strategies for safe and high-performance aqueous zinc-ion batteries: a mini-review, Energy Fuels 38 (2024) 12510–12527, https://doi.org/10.1021/acs.energyfuels.4c02287.

[21] S. Kumar, G. Saeed, L. Zhu, K.N. Hui, N.H. Kim, J.H. Lee, 0D to 3D carbon-based networks combined with pseudocapacitive electrode material for high energy density supercapacitor: a review, Chem. Eng. J. 403 (2021) 126352, https://doi.org/10.1016/j.cej.2020.126352.

[22] S. Jha, B. Akula, P. Boddu, M. Novak, H. Enyioma, R. Cherradi, H. Liang, Roles of molecular structure of carbon-based materials in energy storage, Mater. Today Sustain. 22 (2023) 100375, https://doi.org/10.1016/j.mtsust.2023.100375.

[23] K. Jayaramulu, D.P. Dubal, B. Nagar, V. Ranc, O. Tomanec, M. Petr, K.K.R. Datta, R. Zboril, P.G. Romero, R.A. Fischer, Ultrathin hierarchical porous carbon nanosheets for high-performance supercapacitors and redox electrolyte energy storage, Adv. Mater. 30 (2018) 1705789, https://doi.org/10.1002/adma.201705789.

[24] W. He, J. Duan, H. Liu, C. Qian, M. Zhu, W. Zhang, Y. Liao, Conjugated microporous polymers for advanced chemical sensing applications, Prog. Polym. Sci. 148 (2024) 101770, https://doi.org/10.1016/j.progpolymsci.2023.101770.

[25] H. Sun, W. Chan, H. Zhang, R. Jiao, F. Wang, Z. Zhu, A. Li, Robust synthesis of free-standing films comprising conjugated microporous polymers nanotubes for water disinfection, J. Colloid Interface Sci. 655 (2024) 771–778, https://doi.org/10.1016/j.jcis.2023.11.056.

[26] J. Zhan, A.F.M. EL-Mahdy, Redox-active Benzodithiophene-4, 8-dione-Based conjugated microporous polymers for high-performance faradaic supercapacitor energy storage, Chem. Eng. J. 473 (2023) 145124, https://doi.org/10.1016/j.cej.2023.145124.

[27] Y. Ren, Y. Xu, Recent advances in two-dimensional polymers: synthesis, assembly and energy-related applications, Chem. Soc. Rev. 53 (2024) 1823–1869, https://doi.org/10.1039/d3cs00782k.

[28] Y. Zang, S. Gao, B. Jing, H. Sun, J. Wang, J. Liu, Synthesis of Pd/conjugated microporous polymer heterogeneous catalysts via imine groups and high catalytic efficiency on Suzuki–Miyaura coupling reaction, J. Mater. Sci. 58 (2023) 170–185, https://doi.org/10.1007/s10853-022-08032-8.

[29] G. Feng, Y. Sun, J. Yuan, J. Qian, N. Siam, D. Fa, W. Ji, E. Zhang, Y. Shen, J. Yan, S. Lei, W. Hu, A CMP-based [FeFe]-hydrogenase dual-functional biomimetic system for photocatalytic hydrogen evolution coupled with degradation of tetracycline, Appl. Catal. B Environ. 340 (2024) 123200, https://doi.org/10.1016/j.apcatb.2023.123200.

[30] S. Luo, Z. Zeng, H. Wang, W. Xiong, B. Song, C. Zhou, A. Duan, X. Tan, Q. He, G. Zeng, Z. Liu, R. Xiao, Recent progress in conjugated microporous polymers for clean energy: synthesis, modification, computer simulations, and applications, Prog. Polym. Sci. 115 (2021) 101374, https://doi.org/10.1016/j.progpolymsci.2021.101374.

[31] M. Khakbaz, A. Ghaemi, G.M.M. Sadeghi, Synthesis methods of microporous organic polymeric adsorbents: a review, Polym. Chem. 12 (2021) 6962–6997, https://doi.org/10.1039/d1py01145f.

[32] A. Hayat, M. Sohail, A. El Jery, K.M. Al-Zaydi, S. Raza, H. Ali, Y. Al-Hadeethi, T. A. Taha, I.U. Din, M.A. Khanm, M.A. Amin, E. Ghasali, Y. Orooji, Z. Ajmal, M. Z. Ansari, Recent advances in ground-breaking conjugated microporous polymers-based materials, their synthesis, modification and potential applications, Mater. Today 64 (2023) 180–208, https://doi.org/10.1016/j.mattod.2023.02.025.

[33] H. Li, W. Lyu, Y. Liao, Engineering redox activity in conjugated microporous polytriphenylamine networks using pyridyl building blocks toward efficient supercapacitors, Macromol. Rapid Commun. 40 (2019) 1900455, https://doi.org/10.1002/marc.201900455.

[34] K. Amin, N. Ashraf, L. Mao, C.F.J. Faul, Z. Wei, Conjugated microporous polymers for energy storage: recent progress and challenges, Nano Energy 85 (2021) 105958, https://doi.org/10.1016/j.nanoen.2021.105958.

[35] D. Ai, Y. Han, Z. Xie, X. Pang, Y. Chang, H. Li, C. Wu, Y. Cheng, High temperature polyimide nanocomposites containing two-dimensional nanofillers for improved thermal stability and capacitive energy storage performance, Nano Res. 17 (2024) 7746–7755, https://doi.org/10.1007/s12274-024-6765-4.

[36] R. Kushwaha, S. Dey, K. Gupta, B.B. Mandal, D. Das, Secondary chemical cross-linking to improve mechanical properties in a multifaceted biocompatible strain sensor, ACS Appl. Mater. Interfaces 16 (2024) 5183–5195, https://doi.org/10.1021/acsami.3c18247.

[37] M. Guo, T. Ban, Y. Wang, X. Wang, X. Zhu, 'Thiol-ene' crosslinked polybenzimidazoles anion exchange membrane with enhanced performance and durability, J. Colloid Interface Sci. 638 (2023) 349–362, https://doi.org/10.1016/j.jcis.2023.01.137.

[38] D. Zhou, K. Zhang, S. Zou, X. Li, H. Ma, Conjugated microporous polymers: their synthesis and potential applications in flexible electrodes, J. Mater. Chem. A 12 (2024) 17021–17053, https://doi.org/10.1039/d4ta02085e.

[39] Z. Yu, L. Huang, Z. Sun, F. Cai, M. Liang, Z. Luo, Designing anthraquinone-based conjugated microporous polymers with dual-ion storage behavior towards high-performance lithium-organic batteries, J. Power Sources 550 (2022) 232149, https://doi.org/10.1016/j.jpowsour.2022.232149.

[40] W. Kong, X. Lu, X. Ge, Q. Zhang, X. Jin, M. Zhang, Y. Feng, Conjugated microporous polytriphenylamine as a high-performance anion-capture electrode for hybrid capacitive deionization with ultrahigh areal adsorption capacity, J. Mater. Chem. A 12 (2024) 21124–21133, https://doi.org/10.1039/D4TA04010D.

[41] M.G. Kotp, S.-W. Kuo, A.F.M. EL-Mahdy, Phenazine-based conjugated microporous polymers: influence of planarity and imine content on energy storage performance, Colloids Surfaces A Physicochem. Eng. Asp. 685 (2024) 133210, https://doi.org/10.1016/j.colsurfa.2024.133210.

[42] A. Xie, Z. Ma, Z. Xiong, W. Li, L. Jiang, Q. Zhuang, S. Cheng, W. Lu, Conjugate ferrocene polymer derived magnetic Fe/C nanocomposites for electromagnetic absorption application, J. Mater. Sci. Technol. 175 (2024) 125–131, https://doi.org/10.1016/j.jmst.2023.08.016.

[43] C. Li, D. Kong, B. Wang, H. Du, J. Zhao, Y. Dong, Y. Xie, Conjugated microporous polymer derived N, O and S co-doped sheet-like carbon materials as anode materials for high-performance lithium-ion batteries, J. Taiwan Inst. Chem. Eng. 134 (2022) 104293, https://doi.org/10.1016/j.jtice.2022.104293.

[44] H. Li, F. Pan, C. Qin, T. Wang, K. Chen, Porous organic polymers-based single-atom catalysts for sustainable energy-related electrocatalysis, Adv. Energy Mater. 13 (2023) 2301378, https://doi.org/10.1002/aenm.202301378.

[45] X. Yang, C. Hu, Y. Chen, Z. Song, L. Miao, Y. Lv, H. Duan, M. Liu, L. Gan, Tailoring ion-accessible pores of robust nitrogen heteroatomic carbon nanoparticles for high-capacity and long-life Zn-ion storage, J. Energy Storage 104 (2024) 114509, https://doi.org/10.1016/j.est.2024.114509.

[46] A.F. Saber, S.-W. Kuo, A.F.M. EL-Mahdy, Microporous carbons derived from nitrogen-rich triazatruxene-based porous organic polymers for efficient cathodic supercapacitors, J. Mater. Chem. A 12 (2024) 15373–15385, https://doi.org/10.1039/d4ta01242a.

[47] L. Zhu, Y. Cao, T. Xu, H. Yang, L. Wang, L. Dai, F. Pan, C. Chen, C. Si, Covalent organic framework membranes for energy storage and conversion, Energy Environ. Sci. 18 (2025) 5675–5739, https://doi.org/10.1039/d5ee00494b.

[48] S.R. Alizadeh, M.A. Ebrahimzadeh, Antiviral activities of pyridine fused and pyridine containing heterocycles, a review (from 2000 to 2020), Mini Rev. Med. Chem. 21 (2021) 2584–2611, https://doi.org/10.2174/1389557521666210126143558.

[49] M.R. Biradar, C.R.K. Rao, S.V. Bhosale, S.V. Bhosale, Pyridine-functionalized naphthalene diimide-based cross-linked polymer for efficient supercapacitor applications, Energy Fuels 37 (2023) 11332–11341, https://doi.org/10.1021/acs.energyfuels.3c01177.

[50] I. Messias, M.R. Pinto, A.C. Roveda Jr., A.C. Queiroz, F.H.B. Lima, R. Nagao, Electrochemical mass spectrometry study of the pyridine/pyridinium in the CO_2 electroreduction reaction on copper electrodes, Electrochim. Acta 436 (2022) 141445, https://doi.org/10.1016/j.electacta.2022.141445.

[51] Y. Chen, Z. Song, Y. Lv, L. Gan, M. Liu, NH4$^+$-Modulated cathodic interfacial spatial charge redistribution for high-performance dual-ion capacitors, Nano-Micro Lett. 17 (2025) 117, https://doi.org/10.1007/s40820-025-01660-0.

[52] A.F. Saber, A.F.M. EL-Mahdy, S.-W. Kuo, One-Pot synthesis of heteroatom-rich anthraquinone-based benzoxazine-linked porous organic polymers for high performance supercapacitors, Electrochim. Acta 511 (2025) 145397, https://doi.org/10.1016/j.electacta.2024.145397.

[53] S. Yazar, N. Karahan, M.B. Arvas, Polypyrrole decorated with an anthraquinone dye for energy storage applications, Synth. Met. 297 (2023) 117403, https://doi.org/10.1016/j.synthmet.2023.117403.

[54] T. Qun, T. Zhou, J. Hao, C. Wang, K. Zhang, J. Xu, X. Wang, W. Zhou, Antibacterial activities of anthraquinones: structure–activity relationships and action mechanisms, RSC Med. Chem. 14 (2023) 1446–1471, https://doi.org/10.1039/d3md00116d.

[55] X. Wang, G. Wang, X. He, Anthraquinone porous polymers with different linking patterns for high performance Zinc-Organic battery, J. Colloid Interface Sci. 629 (2023) 434–444, https://doi.org/10.1016/j.jcis.2022.08.166.

[56] X. Li, X. Yin, J. Li, B. Yuan, C. Xiang, P. Zou, L. Wang, Synthesis of coplanar quaternary ammonium salts with excellent electrochemical properties based on an anthraquinone skeleton and their application in copper plating, Electrochim. Acta 437 (2023) 141541, https://doi.org/10.1016/j.electacta.2022.141541.

[57] H. Rzepa, Conformational analysis of biphenyls: an upside-down view, Authorea Prepr. (2015) 1–4, https://doi.org/10.15200/winn.143118.81906.

[58] H. Behmadi, S. Naderipour, S.M. Saadati, M. Barghamadi, M. Shaker, N. Tavakoli-Hoseini, Solvent-free synthesis of new 2,4,6-triarylpyridines catalyzed by a Brønsted acidic ionic liquid as a green and reusable catalyst, J. Heterocycl. Chem. 48 (2011) 1117–1121, https://doi.org/10.1002/jhet.697.

[59] S. Knoll, C. Zens, T. Maisuradze, H. Schmidt, S. Kupfer, L. Zedler, B.D. Ivanšić, C. Streb, Light-Induced charge separation in covalently linked BODIPY-Quinone-Alkyne dyads, Chem. Eur J. 30 (2024) e202303250, https://doi.org/10.1002/chem.202303250.

[60] L. Li, F. Lu, R. Xue, B. Ma, Q. Li, N. Wu, H. Liu, W. Yao, H. Guo, W. Yang, Ultrastable triazine-based covalent organic framework with an interlayer hydrogen bonding for supercapacitor applications, ACS Appl. Mater. Interfaces 11 (2019) 26355–26363, https://doi.org/10.1021/acsami.9b06867.

[61] A.F.M. EL-Mahdy, M.G. Mohamed, T.H. Mansoure, H.-H. Yu, T. Chen, S.-W. Kuo, Ultrastable tetraphenyl-p-phenylenediamine-based covalent organic frameworks as platforms for high-performance electrochemical supercapacitors, Chem. Commun. 55 (2019) 14890–14893, https://doi.org/10.1039/c9cc08107k.

[62] A.F.M. EL-Mahdy, Y.-H. Hung, T.H. Mansoure, H.-H. Yu, T. Chen, S.-W. Kuo, A hollow microtubular Triazine- and Benzobisoxazole-Based covalent organic framework presenting sponge-like shells that functions as a high-performance supercapacitor, Chem. Asian J. 14 (2019) 1429–1435, https://doi.org/10.1002/asia.201900296.

[63] C. Su, H. He, L. Xu, K. Zhao, C. Zheng, C. Zhang, A mesoporous conjugated polymer based on a high free radical density polytriphenylamine derivative: its preparation and electrochemical performance as a cathode material for Li-ion batteries, J. Mater. Chem. A 5 (2017) 2701–2709, https://doi.org/10.1039/c6ta10127e.

[64] W. Liu, M. Ulaganathan, I. Abdelwahab, X. Luo, Z. Chen, S.J.R. Tan, X. Wang, Y. Liu, D. Geng, Y. Bao, J. Chen, K.P. Loh, Two-dimensional polymer synthesized via solid-state polymerization for high-performance supercapacitors, ACS Nano 12 (2018) 852–860, https://doi.org/10.1021/acsnano.7b08354.

[65] M.G. Mohamed, A.F.M. EL-Mahdy, Y. Takashi, S.-W. Kuo, Ultrastable conductive microporous covalent triazine frameworks based on pyrene moieties provide high-performance CO_2 uptake and supercapacitance, New J. Chem. 44 (2020) 8241–8253, https://doi.org/10.1039/d0nj01292k.

[66] S. Cong, J. Chen, L. Wang, L. Lan, Y. Wang, H. Dai, H. Liao, Y. Zhou, Y. Yu, J. Duan, Z. Li, I. McCulloch, W. Yue, Donor functionalization tuning the n-type performance of donor–acceptor copolymers for aqueous-based electrochemical devices, Adv. Funct. Mater. 32 (2022) 2201821, https://doi.org/10.1002/adfm.202201821.

[67] J.W. Jeon, J. Shinb, J. Leea, J.-H. Baika, R.M. Evansc, N.B. McKeowne, T.-H. Kima, J.-C. Leed, S.-K. Kimb, B.G. Kim, Hierarchically structured carbon electrodes derived from intrinsically microporous Tröger's base polymers for high-performance supercapacitors, Appl. Surf. Sci. 530 (2020) 147146, https://doi.org/10.1016/j.apsusc.2020.147146.

[68] Z.-Y. Chen, W.-C. Chen, S.-W. Kuo, Enhanced thermal and porous properties of double-decker-shaped polyhedral silsesquioxane-bismaleimide (DDSQ-BMI) nanocomposites for high-performance CO_2 storage and supercapacitors, Polym. Chem. 15 (2024) 553–564, https://doi.org/10.1039/d3py01115a.

[69] M.G. Kotp, J. Lüder, S.-W. Kuo, A.F.M. EL-Mahdy, Phenazine-integrated conjugated microporous polymers for modulating the mechanics of supercapacitor electrodes, Mater. Adv. 5 (2024) 4142–4150, https://doi.org/10.1039/d3ma00979c.

[70] L. Mei, X. Cui, Q. Duan, Y. Li, X. Lv, H. Wang, Metal phthalocyanine-linked conjugated microporous polymer hybridized with carbon nanotubes as a high-performance flexible electrode for supercapacitors, Int. J. Hydrogen Energy 45 (2020) 22950–22958, https://doi.org/10.1016/j.ijhydene.2020.06.208.

[71] X.-C. Li, Y. Zhang, C.-Y. Wang, Y. Wan, W.-Y. Lai, H. Pang, W. Huang, Redox-active triazatruxene-based conjugated microporous polymers for high-performance supercapacitors, Chem. Sci. 8 (2017) 2959–2965, https://doi.org/10.1039/c6sc05532j.

[72] L. Mei, X. Cui, J. Wei, Q. Duan, Y. Li, Metal phthalocyanine-based conjugated microporous polymer/carbon nanotube composites as flexible electrodes for supercapacitors, Dyes Pigments 190 (2021) 109299, https://doi.org/10.1016/j.dyepig.2021.109299.

[73] M. Shaibani, S.J.D. Smith, P.C. Banerjee, K. Konstas, A. Zafari, D.E. Lobo, M. Nazari, A.F. Hollenkamp, M.R. Hill, M. Majumder, Framework-mediated synthesis of highly microporous onion-like carbon: energy enhancement in supercapacitors without compromising power, J. Mater. Chem. A 5 (2017) 2519–2529, https://doi.org/10.1039/c6ta07098a.

[74] Q. Zhou, G. Lv, H. Li, S. Hu, H. Liu, L. Li, L. He, H. Li, P. Hu, J. Wang, Three-dimensional N, P co-doped graphene hydrogel cathode for zinc-ion hybrid capacitor with high specific capacitance and excellent rate performance, J. Power Sources 623 (2024) 235509, https://doi.org/10.1016/j.jpowsour.2024.235509.

[75] A.E. Allah, F. Mohamed, M.A. Ghanem, A.M. Ahmed, Chemical synthesis and super capacitance performance of novel CuO@ Cu 4 O 3/rGO/PANI nanocomposite electrode, RSC Adv. 14 (2024) 13628–13639, https://doi.org/10.1039/d4ra00065j.

[76] P.N. Singh, M.G. Mohamed, S.V. Chaganti, S.U. Sharma, M. Ejaz, J.-T. Lee, S.-W. Kuo, Rational design of ultrastable conjugated microporous polymers based on pyrene and perylene units as high-performance organic electrode materials for supercapacitor applications, ACS Appl. Energy Mater. 6 (2023) 8277–8287, https://doi.org/10.1021/acsaem.3c01391.

[77] Y. Liao, H. Wang, M. Zhu, A. Thomas, Efficient supercapacitor energy storage using conjugated microporous polymer networks synthesized from Buchwald–Hartwig coupling, Adv. Mater. 30 (2018) 1705710, https://doi.org/10.1002/adma.201705710.

[78] C. Young, J. Kim, Y.V. Kaneti, Y. Yamauchi, One-step synthetic strategy of hybrid materials from bimetallic metal–organic frameworks for supercapacitor applications, ACS Appl. Energy Mater. 1 (2018) 2007–2015, https://doi.org/10.1021/acsaem.8b00103.

[79] V.V. Kondratiev, R. Holze, Intrinsically conducting polymers and their combinations with redox-active molecules for rechargeable battery electrodes: an update, Chem. Pap. 75 (2021) 4981–5007, https://doi.org/10.1007/s11696-021-01529-7.

[80] K. Li, X. Liua, T. Zheng, D. Jiang, Z. Zhou, C. Liu, X. Zhanga, Y. Zhang, D. Losic, Tuning MnO_2 to FeOOH replicas with bio-template 3D morphology as electrodes for high performance asymmetric supercapacitors, Chem. Eng. J. 370 (2019) 136–147, https://doi.org/10.1016/j.cej.2019.03.190.

[81] V.S. Bhat, A. Toghan, G. Hegde, R.S. Varma, Capacitive dominated charge storage in supermicropores of self-activated carbon electrodes for symmetric supercapacitors, J. Energy Storage 52 (2022) 104776, https://doi.org/10.1016/j.est.2022.104776.

[82] Y. Liu, L. Zhou, J. Ouyang, X. Ao, M. Shuang, A.A. Adesina, Electrodeposition nanofabrication of carboxylated carbon nanotubes/α-MnO_2 nanorods/polypyrrole composites as high hybrid capacitance electrodes for efficient U (VI) electrosorption, Sep. Purif. Technol. 334 (2024) 125989, https://doi.org/10.1016/j.seppur.2023.125989.

[83] W. Ji, T.-X. Wang, X. Ding, S. Lei, B.-H. Han, Porphyrin-and phthalocyanine-based porous organic polymers: from synthesis to application, Coord. Chem. Rev. 439 (2021) 213875, https://doi.org/10.1016/j.ccr.2021.213875.

[84] S. Ravuri, A. Al-Othman, S. Al-Asheh, P. Nancarrow, K. Singh, M. Al-Sayah, Tuning the electrochemical potential window of Niobium carbide based electrodes for

symmetric electrochemical supercapacitors, Case Stud. Chem. Environ. Eng. 10 (2024) 100812, https://doi.org/10.1016/j.cscee.2024.100812.

[85] A. Philip, A.R. Kumar, R.K. Edathil, An aqueous symmetric supercapacitor with wide window and high energy density using redox electrode of Cu–Al-layered double hydroxides and λ-manganese dioxide, Environ. Sci. Pollut. Res. 31 (2024) 45295–45309, https://doi.org/10.1007/s11356-024-34138-4.

[86] V.V. Mohan, P.M. Anjana, R.B. Rakhi, One pot synthesis of tungsten oxide nanomaterial and application in the field of flexible symmetric supercapacitor energy storage device, Mater. Today Proc. 62 (2022) 848–851, https://doi.org/10.1016/j.matpr.2022.04.046, 2022.

[87] R. Rohith, A.T. Prasannakumar, V. Manju, M. Thomas, R.R. Mohan, S.J. Varma, An insight into the electrochemical performance of nanostructured V_2O_5 in aqueous neutral electrolytes and fabrication of 2V, high energy density, symmetric supercapacitor, Electrochim. Acta 503 (2024) 144911, https://doi.org/10.1016/j.electacta.2024.144911.

[88] K. Gajewska, A. Moyseowicz, D. Minta, G. Gryglewicz, Effect of electrolyte and carbon material on the electrochemical performance of high-voltage aqueous symmetric supercapacitors, J. Mater. Sci. 58 (2023) 1721–1738, https://doi.org/10.1007/s10853-023-08148-5.

[89] B. Ambrose, K. Nasrin, M. Arunkumar, A. Kannan, M. Sathish, M. Kathiresan, Viologen-based covalent organic polymers: variation of morphology and evaluation of their ultra-long cycle supercapacitor performance, J. Energy Storage 61 (2023) 106714, https://doi.org/10.1016/j.est.2023.106714.

[90] N. An, M. Wei, C. Guo, J. Xin, C. Meng, D. Sun, Y. Lei, Z. Hu, X. Dong, L. Zhao, Integrated N-doped carbon electrodes with regional synergistic energy storage mechanisms for zinc-ion hybrid supercapacitors, J. Power Sources 599 (2024) 234212, https://doi.org/10.1016/j.jpowsour.2024.234212.

[91] S. Mathan, M. Selvaraj, M.A. Assiri, K. Kandiah, R. Rajendran, Synthetic nanoarchitectonics with ultrafast Joule heating of graphene-based electrodes for high energy density supercapacitor application, J. Surf. Interfac. 51 (2024) 104707, https://doi.org/10.1016/j.surfin.2024.104707.

[92] R. Chen, X. Cai, X. He, X. Hong, Y. Liu, J.-K. So, B. Wang, Y. Zhou, L. Cheng, Z. X. Shen, High mass-loading CoO@ NiCo-LDH//FeNiS flexible supercapacitor with high energy density and fast kinetics, Chem. Eng. J. 484 (2024) 149736, https://doi.org/10.1016/j.cej.2024.149736.